Cement & Concrete Composites 33 (2011) 572–585

Contents lists available at ScienceDirect

Cement & Concrete Composites

journal homepage: www.elsevier.com/locate/cemconcomp

Identification of cohesive zone model and elastic parameters of fiber-reinforced cementitious composites using digital image correlation and a hybrid inverse technique

Bin Shen, Glaucio H. Paulino *

Department of Civil and Environmental Engineering, University of Illinois at Urbana–Champaign, Newmark Civil Engineering Laboratory, 205 N. Mathews Avenue, Urbana, IL 61801, USA

ARTICLE INFO

Article history:
Received 26 April 2009
Received in revised form 8 January 2011
Accepted 14 January 2011
Available online 20 January 2011

Keywords:
Cohesive zone model
Inverse problem
Optimization
Nelder–Mead method
Digital image correlation
Identification of elastic moduli
Identification of model parameters
Fracture mechanics
SENB

ABSTRACT

Traditional methods for the inverse identification of elastic properties and local cohesive zone model (CZM) of solids utilize only global experimental data. In contrast, this paper addresses the inverse identification of elastic properties and CZM of a range of materials, using full-field displacement through an optimization technique in a finite element (FE) framework. The new experimental–numerical hybrid approach has been applied to fiber-reinforced cementitious composites (FRCC). PVA microfibers are used at four volume fractions: 0.5%, 1%, 2% and 3%. Digital image correlation (DIC) technique is used to measure surface displacement fields of the test specimens. Four-point bend tests are carried out for the measurement of the modulus of elasticity, E, and the Poisson's ratio, v, while single edge-notched beams (SENB) are used for measurement of mode-I CZM parameters. A finite element update inverse formulation, which is based on minimization of the difference between measured and computed displacement field, is used for both identification problems. For the identification of E and v, linearized form of the Hooke's tensor in plane stress condition has been derived for two-dimensional linear elasticity in FE frame, and Newton–Raphson solver is employed for the inverse problem. For the identification of the CZM, generic spline curves have been used for the parameterization of any CZM thus avoiding the need of an assumption of the CZM shape, while derivative-free Nelder–Mead optimization with CZM shape regularization is employed as the solution method, which reduces the complexity of numerical implementation and improves robustness. The computed E and v are consistent with published results. The computed CZMs of the FRCCs with different fiber volume fractions reveal a strain-hardening characteristic. The computed CZM is used in direct problem simulation, the results of which are consistent with the experimental global response.

1. Introduction

The nonlinear fracture behavior of fiber-reinforced cement composites (FRCC) can be simulated by using the finite element method (FEM). One of the most widely used fracture models is the cohesive zone model (CZM), which is well-suited for FEM implementation [1,2]. CZM is an idealized model to describe the relation between crack surface traction and separation [1,2]. The crack surface separation is also termed crack opening displacement (COD). The traction–separation relation of CZM completely characterizes the local level damage process and the energy dissipation for crack propagation. In many applications, fracture energy and cohesive strength have been regarded as the only two parameters that are needed for a CZM. However, with the fracture energy and the cohesive strength fixed, the softening branch may be represented by various shapes, e.g., the most popularly used are linear, bi-linear or power-law softening curves. Moreover, a few recent studies using FEM have shown that the softening model, i.e., the shape, of the CZM may significantly affect the response of the fracture simulation [3–6]. Therefore, inverse techniques have been developed in order to obtain good estimation of the CZM [7–11], particularly the shape of the CZM.

The traditional inverse techniques for concrete CZM all feature a cost function defining the difference between the measured and the computed load versus crack mouth opening displacement (P-CMOD) curves. A certain shape of the CZM is predefined with a fixed number of model parameters. The CZM parameters are then computed by iteratively updating the CZM parameters until the cost function converges to a minimum. The basic characteristic of this approach is that the global response is used to infer the local constitutive parameters. A recent approach applied to a high explosive (a composite consisting of high volume fraction of energetic

* Corresponding author. Tel.: +1 217 333 3817; fax: +1 217 265 8041.
E-mail address: paulino@illinois.edu (G.H. Paulino).

0958-9465/$ - see front matter © 2011 Elsevier Ltd All rights reserved.
doi:10.1016/j.cemconcomp.2011.01.005

particles in polymeric binder matrix) used the digital image correlation (DIC) to measure the deformation field near the crack surface, multiplied by the bulk elastic modulus, to estimate the cohesive stress. Then by statistically correlating the COD with the cohesive stress, the mode-I cohesive zone model of the local level can be estimated [12]. Although this approach estimates the CZM at a local level, it has been shown in their paper that the data derived for the estimation of the CZM is not smooth due to high noise level in the DIC computed strain.

DIC is a non-contact optical technique that is able to measure two-dimensional as well as three-dimensional surface deformations [13–17]. Essentially, by matching two digital images of the specimen surface, one undeformed and the other deformed, the DIC computes the displacement and/or strain fields. The full field by DIC has been used in fracture mechanics [12,18,19] or in internal defect identification problems [20,21]. It has also been used in the study of the fracture of cementitious materials. For example, it has been used to measure the deformation data of concrete under fracture [22], to study the fracture of quasi-brittle cement paste under compression [23], and to examine the bond between carbon fiber reinforced polymers (CFRP) and concrete substrates [24]. However, it has not been used together with FEM to compute the CZM.

Recently, motivated by the studies reviewed above, the authors of the current paper developed an inverse scheme, which combines the full-field displacement by DIC and inverse analysis in an FEM framework [5,6]. This scheme is used in current study to extract the mode-I CZM for micro fiber-reinforced cement composites (FRCC). With proper material selection and fabrication, FRCC has demonstrated significant enhancement in strength and toughness comparing to pure cement paste, which normally is a brittle material. The strength and toughness enhancement is primarily due to fiber bridging action across cracks forming within the cement matrix. When micro fibers are used in the FRCC, there is a large amount of fibers bridging the crack and the action of the discrete fibers can be smeared into a continuous cohesive stress profile at the crack. Therefore, the CZM can be well applied for the fracture of FRCC.

It may not be apparent that the bulk material properties, particularly the modulus of elasticity, have more pronounced effect on the global response than the shape of the CZM. Fig. 1 shows the P-CMOD responses of three single edge-notched beam (SENB) specimens with the same CZM (shown by the insert) but different bulk elastic moduli. It can be seen that the stiffer the bulk material, the higher the peak load and the steeper the softening curve. Therefore, accurate input of the bulk properties for the finite element model is also important. Usually the basic bulk elastic properties are known or measured by experiments directly. They can also be identified through advanced inverse techniques combined with full-field displacement or strain data [20,21,25]. With full-field displacement data measured by DIC, the finite element model update (FEMU) [21] method is adapted in this study to compute the modulus of elasticity and Poisson's ratio simultaneously.

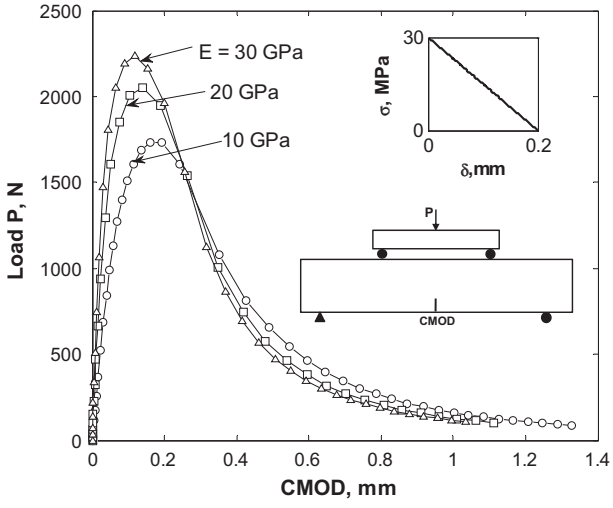

Fig. 1. Effect of the bulk stiffness on the global P-CMOD response (from numerical modeling).

In the following sections, first the inverse problems for identification of elastic moduli and for the computation of mode-I CZM will be defined. Next, the experimental details and procedures are described. Then the results and discussion for the two inverse problems are presented in two consecutive sections. Finally, some concluding remarks are drawn.

2. Inverse identification problems

The FEM representation of the field equations for the general elastostatic problem, based upon the principle of virtual work, is

$$\int_{\Omega} \delta\boldsymbol{\varepsilon} : \mathbf{H} : \boldsymbol{\varepsilon}\, d\Omega - \int_{\Gamma} \boldsymbol{\tau} \cdot \delta\mathbf{u}\, d\Gamma = 0, \tag{1}$$

where Ω is the domain of the solid, Γ is the boundary with known tractions, $\boldsymbol{\varepsilon}$ is the strain tensor, $\boldsymbol{\tau}$ is the vector of tractions, $\mathbf{u}$ is the vector of displacement, and $\mathbf{H}$ is the Hooke's tensor. The Galerkin discretization procedure that uses FEM shape functions can be applied, which leads to the standard FEM system of equations in the form

$$\mathbf{K}_{\mathrm{b}}(\mathbf{H})\mathbf{u} = \mathbf{f}, \tag{2}$$

where $\mathbf{K}_{\mathrm{b}}$ is the bulk stiffness matrix, which is a function of $\mathbf{H}$, $\mathbf{u}$ here is the generalized global displacement vector and $\mathbf{f}$ is the generalized global force vector. Usually $\mathbf{H}$ is known, and solving Eq. (2) for $\mathbf{u}$ constitutes a direct problem.

For the case of nonlinear fracture using CZM, one additional term is added to the direct problem statement of Eq. (1) [26]:

$$\int_{\Omega} \delta\boldsymbol{\varepsilon} : \mathbf{H} : \boldsymbol{\varepsilon}\, d\Omega - \int_{\Gamma} \boldsymbol{\tau} \cdot \delta\mathbf{u}\, d\Gamma - \int_{\Gamma_{coh}} \mathbf{T}_{coh} \cdot \delta\Delta\mathbf{u}\, d\Gamma_{coh} = 0, \tag{3}$$

where Γ_{coh} represents the cohesive surface where the cohesive traction $\mathbf{T}_{coh}$ and the crack opening displacement (COD) $\Delta\mathbf{u}$ are present. Eq. (2) is then updated

$$[\mathbf{K}_{\mathrm{b}}(\mathbf{H}) + \mathbf{K}_{\mathrm{c}}(\boldsymbol{\alpha}, \mathbf{u})]\mathbf{u} = \mathbf{f}, \tag{4}$$

where $\mathbf{K}_{\mathrm{c}}$ is the cohesive stiffness matrix accounting for the contribution from the cohesive traction and depends on the particular CZM defined, $\boldsymbol{\alpha}$ is the vector that defines the CZM. In a fracture simulation, $\{\mathbf{H}; \boldsymbol{\alpha}\}$ is known and the problem is solved for $\mathbf{u}$. Notice that the direct problem of (2) is linear, while (4) is nonlinear because the total stiffness matrix now implicitly depends on $\mathbf{u}$.

When the whole or part of the field of $\mathbf{u}$ can be measured through experiments, e.g., the DIC in this study, the identification of either $\mathbf{H}$ or $\boldsymbol{\alpha}$ becomes inverse problems. In the following, the identification problems for Hooke's tensor and the CZM are developed separately in Sections 2.1 and 2.2.

2.1. Identification of the Hooke's tensor

The FRCC beams tested in this study can be regarded as a two-dimensional (2D) under plane stress condition. It is also appropriate to approximate the FRCC as an isotropic, homogeneous and linear elastic body. The following developments of the inverse problems are based on these assumptions.

2.1.1. Linearization of Hooke's tensor

Starting from a general description, we assume that the Hooke's tensor $\mathbf{H}$, depends on N constitutive parameters in vector form $\boldsymbol{\theta} = \{\theta_1, \ldots, \theta_N\}$, and thus $\mathbf{H} = \mathbf{H}(\boldsymbol{\theta})$. Usually the Hooke's tensor can be decomposed as a linear combination of all the independent scalar moduli

$$\mathbf{H} = \sum_{i=1}^{N} \theta_i \mathbf{H}_i. \tag{5}$$

The standard FEM system of equations for elastic problems can now be expressed as

$$\mathbf{K}_b(\mathbf{H}(\boldsymbol{\theta}))\mathbf{u} = \mathbf{f}. \tag{6}$$

With the decomposed Hooke's tensor, the global stiffness matrix can be set in the form

$$\mathbf{K}_b(\mathbf{H}(\boldsymbol{\theta})) = \mathbf{K}_b\left(\sum \theta_i \mathbf{H}_i\right) = \theta_i \widetilde{\mathbf{K}}_i(\mathbf{H}_i). \tag{7}$$

Apparently,

$$\widetilde{\mathbf{K}}_i(\mathbf{H}_i) = \frac{\partial \mathbf{K}_b}{\partial \theta_i}, \tag{8}$$

which is the sensitivity of $\mathbf{K}_b$ with regard to θ_i. The convenient form of (7) will facilitate the inverse identification procedure.

Now consider the case of a homogeneous, isotropic material, the elastic properties can be described in terms of the Lamé constants λ and μ, in the linearized form as

$$\sigma_{ij} = \lambda \varepsilon_{kk}\delta_{ij} + 2\mu\varepsilon_{ij}, \quad \text{in } \Omega, \tag{9}$$

which is a specific case of Eq. (5). The Lamé's first parameter, λ, can be expressed by

$$\lambda = \frac{Ev}{(1+v)(1-2v)}, \tag{10}$$

and the Lamé's second parameter by

$$\mu = \frac{E}{2(1+v)}, \tag{11}$$

which is the shear modulus. It may not be apparent that the linearized form described by Eq. (9) can only directly apply to 3-D condition. For plane stress condition, the form is different, which is derived as the follows.

For plane stress condition, there is $\sigma_{23} = \sigma_{31} = \sigma_{33} = 0$. From $\sigma_{33} = 0$ and Eq. (9), one obtains

$$\varepsilon_{33} = -\frac{\lambda(\varepsilon_{11} + \varepsilon_{22})}{\lambda + 2\mu}. \tag{12}$$

Therefore, the Hooke's law for isotropic material in plane stress condition can be written explicitly as [5]

$$\begin{Bmatrix} \sigma_{11} \\ \sigma_{22} \\ \sigma_{12} \end{Bmatrix} = \left(2\mu \begin{bmatrix} 2 & 1 & 0 \\ 1 & 2 & 0 \\ 0 & 0 & 1 \end{bmatrix} - \frac{4\mu^2}{\lambda + 2\mu} \begin{bmatrix} 1 & 1 & 0 \\ 1 & 1 & 0 \\ 0 & 0 & 0 \end{bmatrix} \right) \begin{Bmatrix} \varepsilon_{11} \\ \varepsilon_{22} \\ \varepsilon_{12} \end{Bmatrix}. \tag{13}$$

According to Eq. (5), one can define

$$\theta_1 = 2\mu, \quad \theta_2 = -4\mu^2/(\lambda + 2\mu),$$

and

$$\mathbf{H}_1 = \begin{bmatrix} 2 & 1 & 0 \\ 1 & 2 & 0 \\ 0 & 0 & 1 \end{bmatrix}, \quad \mathbf{H}_2 = \begin{bmatrix} 1 & 1 & 0 \\ 1 & 1 & 0 \\ 0 & 0 & 0 \end{bmatrix}.$$

2.1.2. Newton–Raphson optimization

In using the displacement-based optimization approach [5,6,21], a widely used cost function is defined as

$$\Phi(\boldsymbol{\theta}) = \frac{1}{2}(\mathbf{u}^*(\boldsymbol{\theta}) - \bar{\mathbf{u}})^T(\mathbf{u}^*(\boldsymbol{\theta}) - \bar{\mathbf{u}}). \tag{14}$$

where $\mathbf{u}^*$ is the computed displacement vector, which is obtained from the direct problem defined by Eq. (2), assuming that the parameters $\boldsymbol{\theta}$ of Hooke's tensor are known, and $\bar{\mathbf{u}}$ is the displacement field measured from DIC. The minimization of (14) yields estimates of θ. The Newton–Raphson algorithm can be applied with its standard form for minimization:

$$\nabla^2\Phi(\boldsymbol{\theta}_0)\Delta\boldsymbol{\theta} = -\nabla\Phi(\boldsymbol{\theta}_0), \tag{15}$$

where $\boldsymbol{\theta}_0$ is the initial guess of $\boldsymbol{\theta}$, $\Delta\boldsymbol{\theta}$ is the update, $\nabla\Phi$ and $\nabla^2\Phi$ are the gradient and Hessian of Φ, respectively. Starting from a good initial guess $\boldsymbol{\theta}_0$, the iteratively updated $\boldsymbol{\theta}_0$ will eventually converges to the correct estimation. With the linearized form (5), the gradient and Hessian of $\Phi(\boldsymbol{\theta})$ can be derived analytically:

$$\nabla\Phi = \nabla\mathbf{u}^*(\mathbf{u}^* - \bar{\mathbf{u}}), \tag{16}$$

$$\nabla^2\Phi = (\nabla^2\mathbf{u}^*)(\mathbf{u}^* - \bar{\mathbf{u}}) + (\nabla\mathbf{u}^*)(\nabla\mathbf{u}^*)^T. \tag{17}$$

where each component of $\nabla\mathbf{u}^*$, i.e., $\partial\mathbf{u}^*/\partial\theta_i$, can be derived using (2) and (5), i.e.,

$$\frac{\partial\mathbf{u}^*}{\partial\theta_i} = \frac{\partial\mathbf{K}^{-1}\mathbf{f}}{\partial\theta_i} = -\mathbf{K}^{-1}\widetilde{\mathbf{K}}_i\mathbf{K}^{-1}\mathbf{f} = -\mathbf{K}^{-1}\widetilde{\mathbf{K}}_i\mathbf{u}^*. \tag{18}$$

Furthermore, each component of $\nabla^2\mathbf{u}^*$, explicitly as $\partial^2\mathbf{u}^*/\partial\theta_i\partial\theta_j$, can also be derived

$$\frac{\partial^2\mathbf{u}^*}{\partial\theta_i\partial\theta_j} = \mathbf{K}^{-1}\widetilde{\mathbf{K}}_j\mathbf{K}^{-1}\widetilde{\mathbf{K}}_i\mathbf{u}^* + \mathbf{K}^{-1}\widetilde{\mathbf{K}}_i\mathbf{K}^{-1}\widetilde{\mathbf{K}}_j\mathbf{u}^*. \tag{19}$$

2.2. Identification of the CZM model parameters

Fig. 2 shows the finite element model implementing the CZM for a SENB specimen, where $\mathbf{f}_c^e$ is the elemental equivalent cohesive nodal force vector due to cohesive traction, $\mathbf{N}$ is the vector of shape functions, t is the specimen thickness and η is the isoparametric coordinate. According to Fig. 2, now the finite element formulation for the CZM, Eq. (4), can be rewritten as

$$\mathbf{K}_b\mathbf{u} = \mathbf{f} - \mathbf{f}_c(\bar{\mathbf{u}};\boldsymbol{\alpha}), \tag{20}$$

where $\mathbf{f}_c$ is the global force vector contributed by the cohesive traction only. The use of $\mathbf{f}_c$ rather than $\mathbf{K}_c$ is to facilitate the computation of the displacement vector $\mathbf{u}^*$:

$$\mathbf{u}^*(\boldsymbol{\alpha}) = \mathbf{K}_b^{-1}[\mathbf{f} - \mathbf{f}_c(\bar{\mathbf{u}};\boldsymbol{\alpha})]. \tag{21}$$

The bulk material moduli $\boldsymbol{\theta}$ computed from elastic test can be readily used in the inverse problem for the identification of the CZM model parameters. The same cost function as (14) can be used

$$\Phi(\boldsymbol{\alpha}) = \frac{1}{2}(\mathbf{u}^*(\boldsymbol{\alpha}) - \bar{\mathbf{u}})^T(\mathbf{u}^*(\boldsymbol{\alpha}) - \bar{\mathbf{u}}), \tag{22}$$

but now the CZM parameters, $\boldsymbol{\alpha}$, are sought. Notice that H is ignored in Eqs. (20)–(22) because it is known in the inverse problem. The nonzero terms in $\mathbf{f}_c$ are only those DOFs associated with the nodes at the crack surface, which is a small fraction of the total DOFs of $\mathbf{f}_c$. Therefore, the updating of $\mathbf{f}_c$ each time $\boldsymbol{\alpha}$ is updated is not computationally expensive.

2.2.1. Parameterization of the CZM

A unique feature of the proposed inverse scheme is that the CZM is defined using flexible linear or cubic splines with nearly arbitrary number of control points. Fig. 3 shows the parameterization of the CZM curve through a spline, where P_i are the control points, δ_i are the CODs and σ_i are the tractions. The CZM model

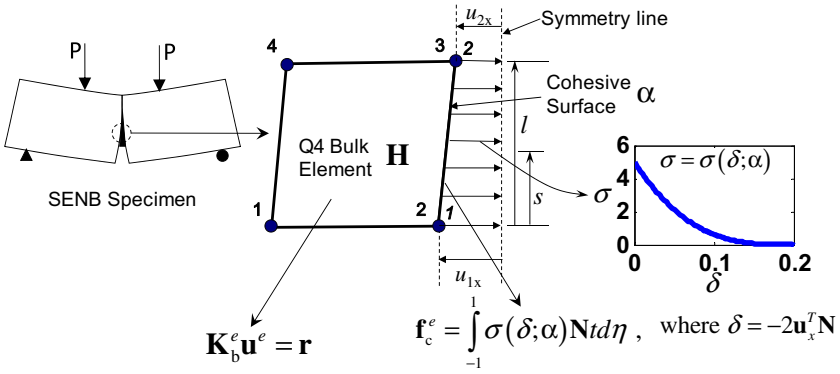

Fig. 2. Finite element implementation of the CZM for a SENB specimen.

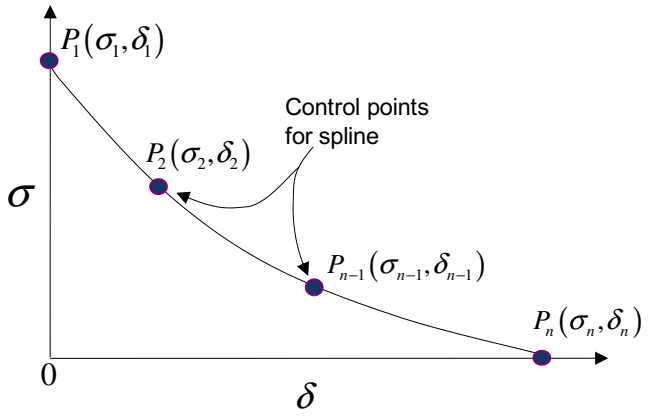

Fig. 3. Parameterization of extrinsic CZM curve using a spline.

parameters are then associated with the control points of the spline:

$$\{\sigma_1,\delta_1,\cdots,\sigma_n,\delta_n\}. \tag{23}$$

Apparently, in the feasible region for (23) the COD must be positive and the traction must be tensile. Another requirement is that the control points' COD ordinate must be sequential, i.e., $0=\delta_1<\delta_2<\cdots<\delta_n$, so that the curve can be constructed. The spline representation allows no presumption of the shape of the CZM for the inverse problem, i.e., the model definition is generic. Such definition of CZM allows the application of the inverse scheme to a variety of materials. One superior advantage of the spline construction of CZM shape is that, theoretically, arbitrary number of control points can be employed depending on the complexity of the expected CZM shape. However, numerically, as the number of control points, i.e., proportionally the number of variables, increases, it will be more and more difficult to solve for the variables. If a robust and tolerant inverse algorithm is employed, more control points can be used for the CZM spline and still be solved.

2.2.2. Nelder–Mead optimization

Newton-like optimization methods can be used for Eq. (22), which require the computation of at least the gradient of the cost function. In addition, different from the identification of the elastic moduli $\boldsymbol{\theta}$, usually it is hard to have a good initial guess of CZM. Many Newton-like methods fail when an initial guess is too far from the final solution. Due to these reasons, the derivative-free Nelder–Mead (N–M) nonlinear optimization method is adapted [27–29].

The derivative-free feature of N–M method means that only the values of the cost function is needed for the progression of the algorithm. This facilitates the implementation of the inverse problem formulated by (22). However, because the N–M method is also an unconstrained optimization method, the feasibility of the CZM parameters has to be enforced. These can be done by introducing the barrier terms into the cost function

$$\Phi(\boldsymbol{\alpha})=\frac{1}{2}(\mathbf{u}^*(\boldsymbol{\alpha})-\bar{\mathbf{u}})^T(\mathbf{u}^*(\boldsymbol{\alpha})-\bar{\mathbf{u}})+\beta_1(\boldsymbol{\alpha})+\beta_2(\boldsymbol{\alpha}), \tag{24}$$

where $\beta_1(\boldsymbol{\alpha})$ and $\beta_2(\boldsymbol{\alpha})$ are the barrier terms defined as follows:

$$\beta_1(\boldsymbol{\alpha})=\sum_i 10^{N_b(\theta_b-\sigma_i)/\theta_b}, \tag{25}$$

where $0<\theta_b\ll 1$, and $N_b\gg 1$ is used to penalize $\Phi(\boldsymbol{\alpha})$ if $\alpha_i\leqslant 0$.

$$\beta_2(\boldsymbol{\alpha})=\sum_i 10^{N_b\{[\xi_i-(1-\theta_b)]/\theta_b\}}, \tag{26}$$

where

$$\xi_i=\left|\frac{\delta_{n,i}-(\delta_{n,i-1}+\delta_{n,i+1})/2}{(\delta_{n,i+1}-\delta_{n,i-1})/2}\right|, \tag{27}$$

is the normalized horizontal distance of point i from the midpoint of the adjacent two points $i-1$ and $i+1$ (see Fig. 4). When $\xi_i<1$, condition $\delta_{n,i-1}<\delta_{n,i}<\delta_{n,i+1}$ is satisfied. When $\xi_i>1-\theta_b$, a numerical penalty appears. Thus the requirement that $\delta_1<\delta_2<\cdots<\delta_n$ can be ensured during optimization. One example of the barrier term $\beta_1(\boldsymbol{\alpha})$ is illustrated in Fig. 5. The barrier term $\beta_2(\boldsymbol{\alpha})$ has the same effect as $\beta_1(\boldsymbol{\alpha})$ and is not shown.

The regularization of the CZM shape is realized by monitoring the CZM shape during the optimization iterations. Several criteria are defined to detect if the CZM shape computed shows clustered, spike or tail points. Once detected, the optimization can be halted. The locations of control points are redistributed so that those situations are removed but the major curve shape is maintained. The optimization is then restarted with a set of better-estimated and well-conditioned initial guess. For the details of this regularization, the readers are referred to [5,30].

2.2.3. Formation of cohesive zone

To solve for cohesive parameters $\boldsymbol{\alpha}$ from Eq. (22), a complete cohesive zone must be assured at the load level when the displacement $\bar{\mathbf{u}}$ is measured by DIC, so that every parameter in $\boldsymbol{\alpha}$ is active for the computation of $\mathbf{u}^*$. Intuitively, one might think the com-

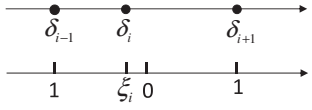

Fig. 4. Normalized COD distance of point i from the middle of two adjacent points.

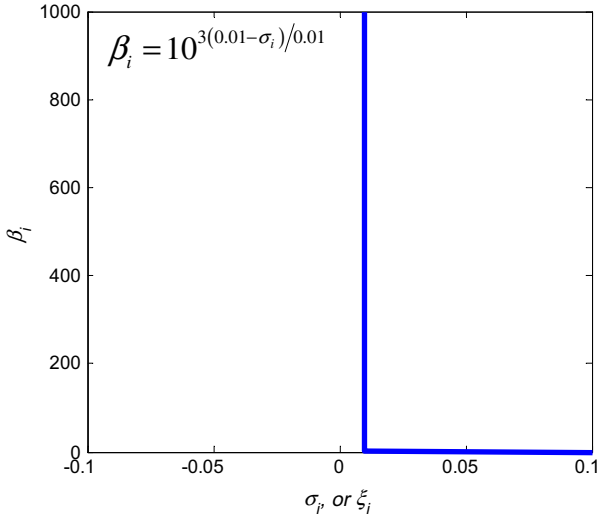

Fig. 5. Illustration of a barrier term.

plete cohesive zone forms at or around peak load. However, it has been demonstrated by Park et al. [31] that the complete cohesive zone for a fiber-reinforced concrete SENB specimen may not form at peak load level but rather at a post-peak load level. In their study, a bilinear softening CZM is used for the mode I fracture of concrete. To estimate the critical load levels where the complete cohesive zone forms for the examples in this study, the cohesive stress distribution can be plotted along the crack path and direct inspection can provide the estimation. In the following, qualitative estimations for the threshold load levels are made by FEM simulation for the model shown in Fig. 6, where two CZMs are investigated: one with a hardening behavior and one with a linear softening behavior.

Fig. 7 illustrates the formation of cohesive zone for the softening CZM case. In the figure, the cohesive stress profiles are plotted along the crack at pre-peak load, peak load, and post-peak load levels. The crack is located from $x = 5.5$ mm to $x = 25.5$ mm. Fig. 8 illustrates the formation of cohesive zone for the hardening CZM case. When the COD at initial crack tip reaches the critical separation, δ_c, the corresponding traction at initial crack tip drops to zero.

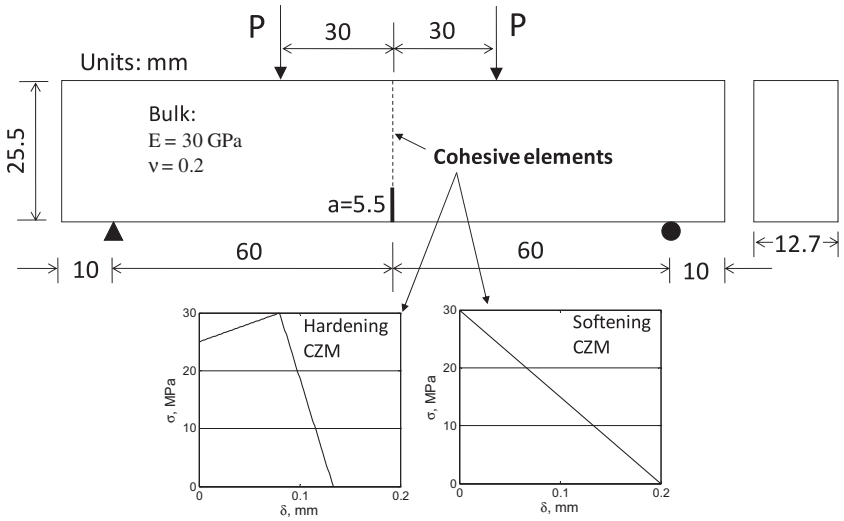

Fig. 6. FEM model for the estimation of the load levels when the complete cohesive zone forms. Both hardening and softening CZMs are used in the fracture simulation.

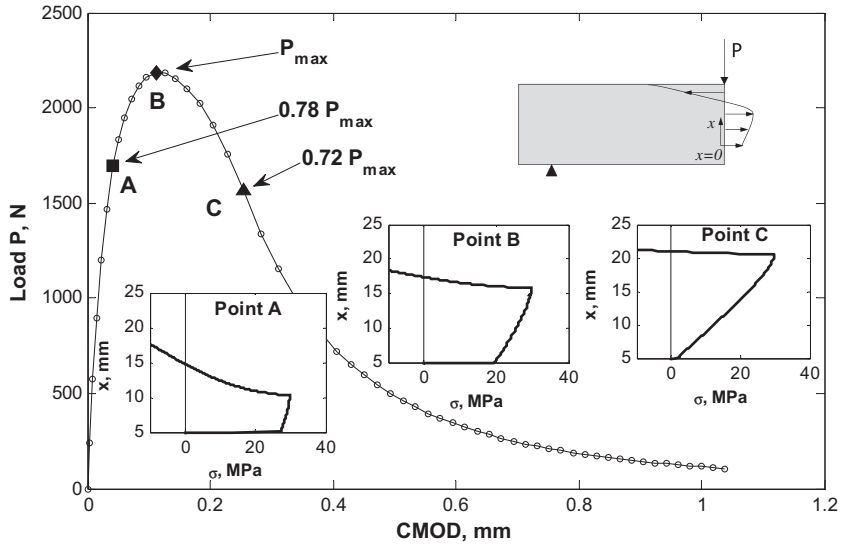

Fig. 7. Illustration of the formation of cohesive zone for linear CZM at different points: at pre-peak load level "A", at peak load level "B", and at post-peak load level "C".

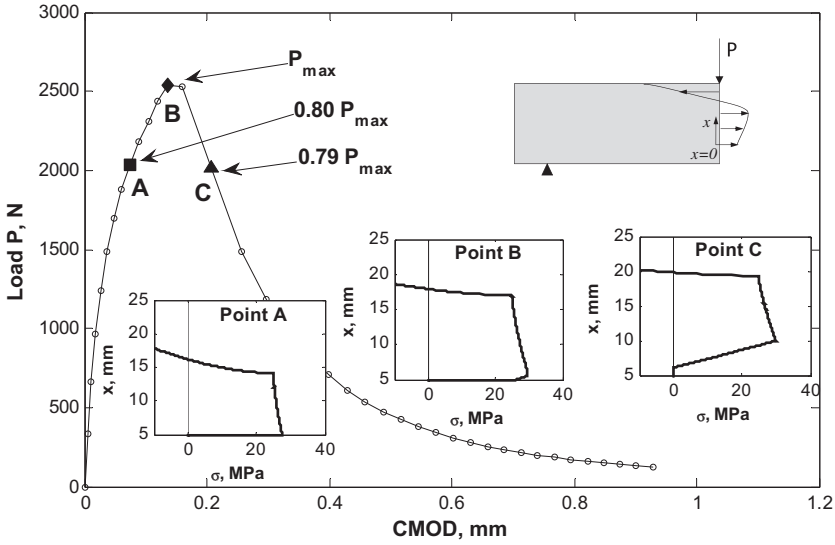

Fig. 8. Illustration of the formation of cohesive zone for hardening CZM at different points: at pre-peak load level "A", at peak load level "B", and at post-peak load level "C".

At this moment, a complete cohesive zone first forms behind the initial crack tip. From both figures, it can be seen only at load level "C" does the complete cohesive zone forms. For linear CZM, this point corresponds to 70% of the post-peak load level, while for hardening CZM, the threshold is at about 80% of the post-peak load level. Therefore, displacement data at a post-peak load level shall be used in the inverse analysis.

3. Experimental program

The procedure described in [32] is used to prepare the FRCC specimens for bending and fracture tests, as well as DIC measurement. The nominal specimen dimensions for both the bending and fracture test specimens are $26 \times 13 \times 140$ mm (height $\times$ width $\times$ length). For the single edge-notched beam (SENB) specimen for fracture testing, the nominal notch size is 6 mm. Four different fiber volume fractions are used: 0.5%, 1%, 2% and 3%. The mix proportions for the specimens are presented in Table 1.

Black and white enamel-based paints are used to prepare the speckle pattern for DIC. A Paasche® Single Action – External Mix – Siphon Feed Airbrushes is used to first spray white paint on the specimen as background. The amount of white paint sprayed is just enough to uniformly and fully cover the specimen. Then black paint is sprayed to generate the random speckle pattern. Fig. 9 shows a typical speckle pattern generated for DIC.

The setup of four-point pure bending test is shown in Fig. 10. The region defined by the dashed line indicates the region of interest (ROI) where the displacement is computed by DIC.

The setup of the fracture testing is similar to the setup of the bend test, except the SENB specimen is used instead and CMOD is used as the control channel. Due to heterogeneity, the FRCC SENB specimen may not show straight crack paths. Thus, a shallow straight groove on both sides of the specimens is introduced to confine the crack path within the groove (Fig. 11). The grooves are made by a specially tailored thin band saw. All groove depth from the surface are between 1 and 1.5 mm. The initial notch size, a_0, is 6 ± 0.3 mm.

4. Identification of the elastic moduli

While conventional experimental methods usually determine one or two elastic properties from a single experiment using the global response data, the theory presented in Section 2.1 shows that the complete Hooke's tensor, i.e., all elastic properties, can be computed utilizing full-field displacement data in a single load test. This section presents the results computed from the hybrid DIC-FEM inverse technique.

The loading of the FRCC 4-point bending test is displacement (crosshead) controlled at a rate of 0.2 mm/min. The load versus crosshead displacement curves for the four FRCCs are shown in Fig. 12, all show initial linear response followed by nonlinear responses after cracking occurs. Depends on the amount of fibers, the post-cracking response can be softening only (0.5% FRCC), or hardening (1–3% FRCC). Notice for 2% and 3% FRCCs, the ratios of the limit of linearity to the ultimate/peak strength are relatively small, which indicates that the fibers are carrying significant post-cracking load. Multiple DIC images are taken for each specimen. However, only the DIC images taken before cracking can be used to measure the elastic moduli due to the continuous assumption of the DIC algorithm. The load levels when the DIC images taken shall not be too small, so that sufficient elastic deformation can

Table 1
Mix proportions of FRCCs with different fiber volume fraction.

Cement (wt.)	Fly ash class *F* (wt.)	Water (wt.)	Fiber (vol.%)	Superplasticizer[a] (wt.)	HPMC[b]/water (wt.)
0.573	0.427	0.210	0.5	0.002	0.04
		0.215	1		
		0.220	2		
		0.225	3		

[a] Effective weight of superplasticizer (Grace Advance Flow).
[b] HPMC: hydroxypropyl methylcellulose.

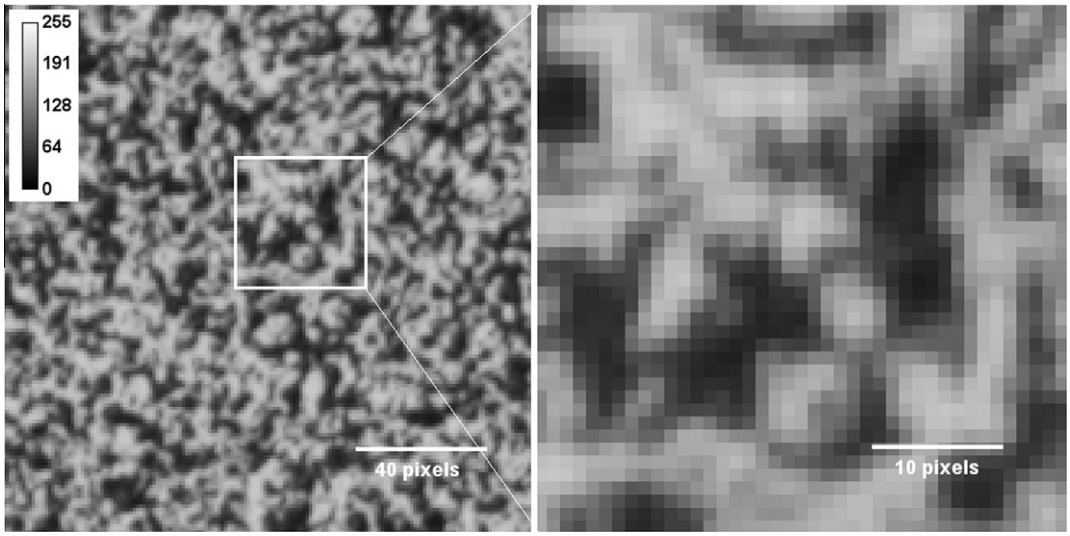

Fig. 9. A typical speckle pattern used in DIC.

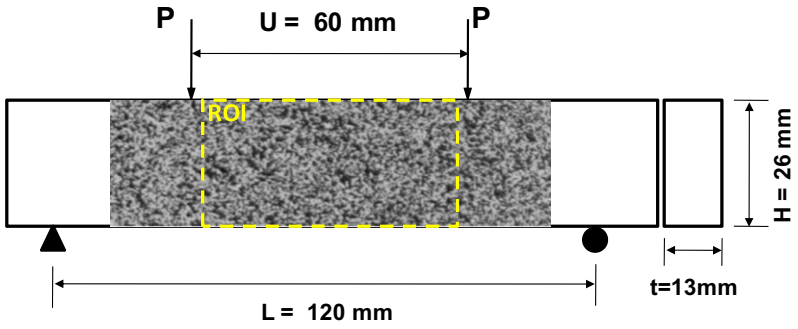

Fig. 10. Bending test setup, the rectangle is the region of interest (ROI) where the DIC displacement is computed.

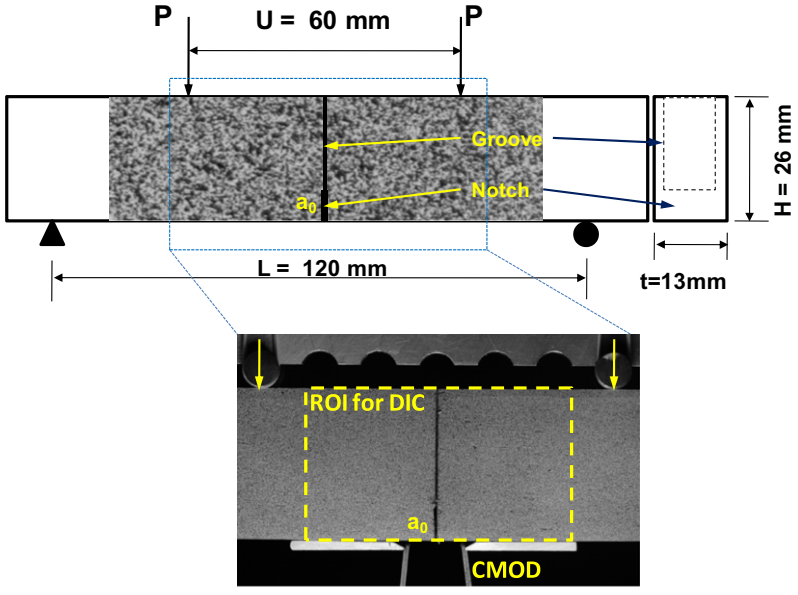

Fig. 11. Fracture test setup (upper: schematic, lower: actual image). The rectangle is the region of interest (ROI) where the DIC displacement is computed – notice the profile of the groove and notch.

be accurately measured. In addition to the reference image taken at zero loading, two images at different elastic load levels are used for each specimen. The load levels corresponding to the images used for DIC are listed in Table 2.

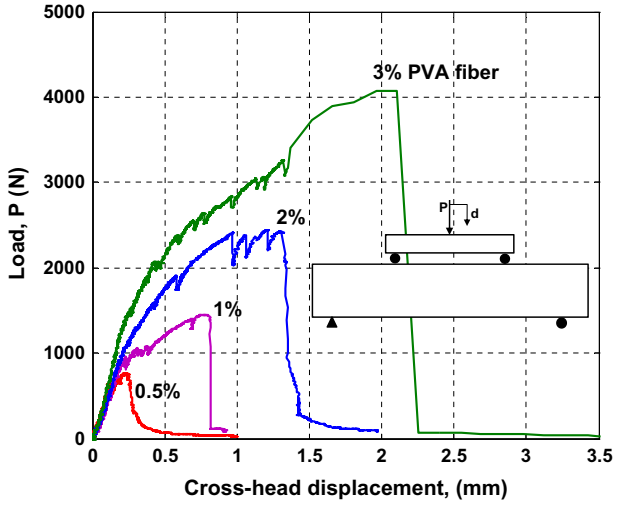

Fig. 12. Load versus displacement curves for FRCCs with various fiber volume fractions.

Table 2
Loadings when specimen images are taken for DIC, in N (note: FRCC-0.5 means the FRCC has 0.5% fiber volume fraction, same for the remaining specimen IDs).

	Reference point	Deform 1	Deform 2
FRCC-0.5	0	440	585
FRCC-1	0	480	723
FRCC-2	0	597	866
FRCC-3	0	596	992

The full-field DIC is used to measure the displacement field within the region of interest (Fig. 10). A typical displacement field is shown in Fig. 13, with DIC resolution equals 17.6 μm/pixel. Notice the very small displacement variation over the region of interest: 1.9 pixels over a width of 3414 pixels for u_x and 1.3 pixels over a height of 1480 pixels. The corresponding maximum compression or tension strain at top or bottom fibers is 0.56×10^{-3}. Using 0.05 pixel as the conservative estimation for the resolution of DIC used in this study, the estimated relative error for the strain measurement will be ±0.05/1.9 = ±2.6% for ε_x, and ± 0.05/1.3 = ±3.8% for ε_y.

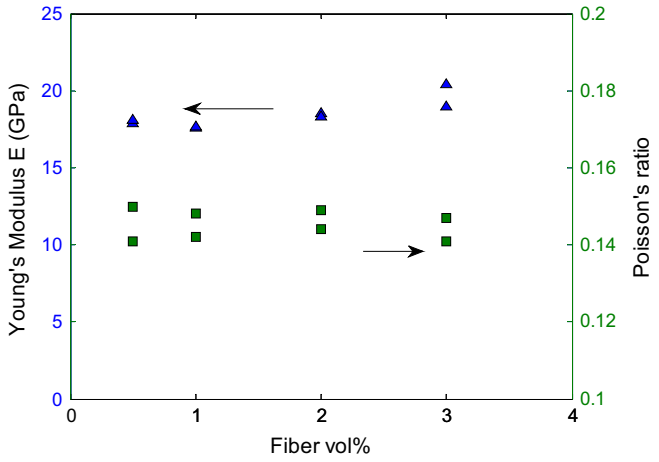

Fig. 14. The computed Young's modulus and Poisson's ratio versus fiber volume fraction.

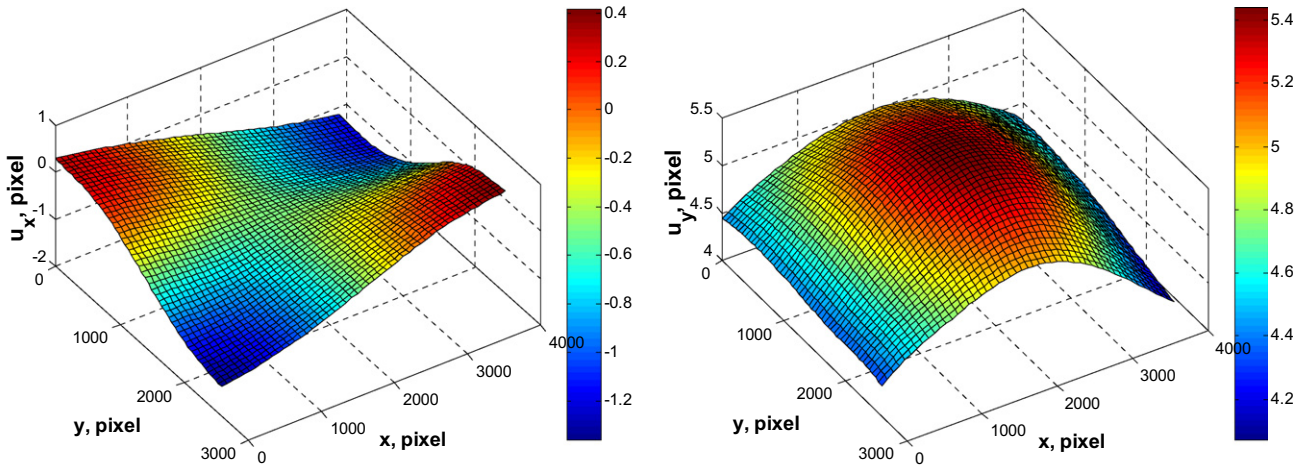

Fig. 13. Surface plot of displacement field u_x and u_y by DIC for FRCC-3 bending specimen at $P = 992$ N.

Table 3
The inverse computation of isotropic elastic properties.

	Initial guess		Load level (N)	Converged results		$\Phi(\theta^{(0)})$	$\Phi(\theta^{(n)})$	# of iterations
	E (GPa)	ν		E (GPa)	ν			
FRCC-0.5	10.0	0.2	440	17.9	0.150	0.0015	0.000212	11
			585	18.1	0.141	0.0033	0.000376	16
FRCC-1	10.0	0.2	480	17.6	0.148	0.0019	0.000293	10
			723	17.7	0.142	0.0043	0.000540	15
FRCC-2	10.0	0.2	597	18.5	0.149	0.0029	0.000411	9
			866	18.3	0.144	0.0068	0.000798	14
FRCC-3	10.0	0.2	596	19.0	0.147	0.0032	0.000446	8
			992	20.4	0.141	0.0106	0.000825	12

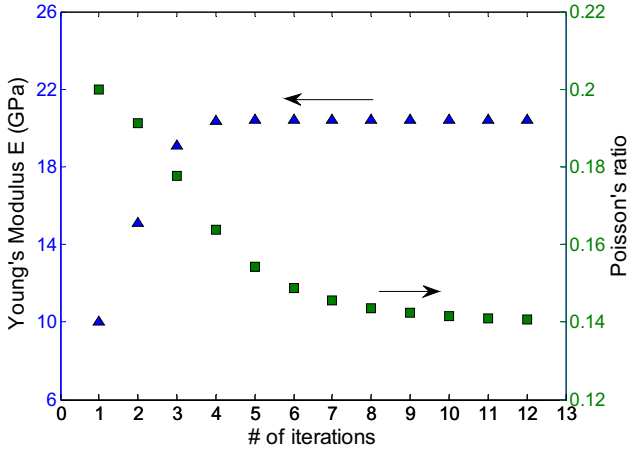

Fig. 15. Evolution of the computation of Young's modulus and Poisson's ratio for FRCC-3 specimen with DIC taken at a load of 992 N.

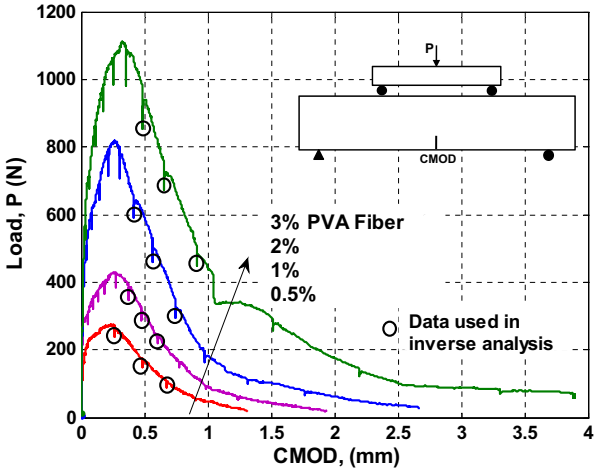

Fig. 16. Load versus CMOD for FRCC with various fiber volume fractions.

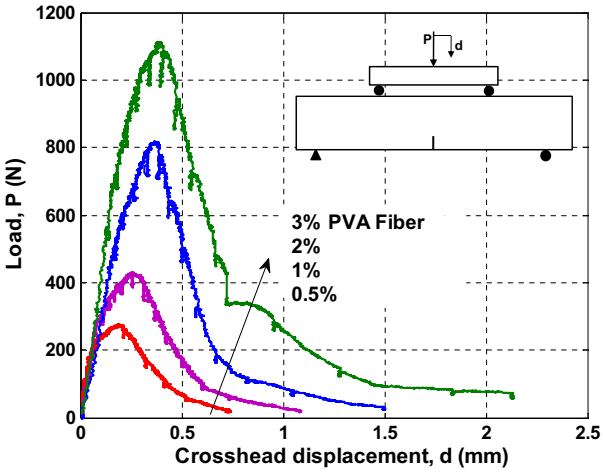

Fig. 17. Load versus load–line displacement for FRCC with various fiber volume fractions.

This bound of relative error estimates will translate to the final error of the computed elastic properties.

Initial guess of $E = 10$ GPa and $\nu = 0.2$ are assumed for the Newton–Raphson procedure described previously. The inversely computed properties can be obtained in a few iterations. The computed properties, as well as the initial and final values of the cost function, and the number of iterations for convergence are summarized in Table 3. The computed Young's moduli and Poisson's ratios are also shown in Fig. 14. For each specimen, the computed E and ν are accurate: the difference computed at the two different loads for the same specimen is less than 7% for E and 6% for ν. The Poisson's ratios computed from higher load data are consistently lower than those computed from lower load data. The value of the lower Poisson's ratio may be more accurate because higher deformation at higher loads reduces the relative DIC measurement errors. The presence of PVA fibers does not affect the bulk elastic properties, which is expected. The PVA fiber has a Young's modulus of 39 GPa[1], while the ordinary cement paste modulus is in the range of 10–20 GPa [33,34].

Ref. [35] has reported a 2% PVA FRCC with a 20.3 GPa Young's modulus and Ref. [36] has reported 18.7 GPa for a 2.8% PVA ECC. However, both references do not provide the measurement for Poisson's ratio. It has been generally accepted that concrete has a Poisson's ratio between 0.15 and 0.2 [33,34], depending on the mix proportion. The FRCC is primarily composed of cementitious matrix, thus the lower-end Poisson's ratio, ~0.15, shall be expected for FRCC. This correlates very well with the computed Poisson's ratios.

The convergence rate of Newton–Raphson algorithm is very fast. An illustration of a typical evolution of the E and ν during optimization is shown in Fig. 15, for the FRCC-3 specimen at the higher load. As can be seen, the convergence of ν is slower than the convergence of E. The horizontal displacement is almost solely sensitive to E while the variation of vertical displacement is sensitive only to ν.

In the subsequent computation of the FRCC cohesive properties, the average of E and ν computed at two loads for each FRCC are used. As will be shown, the dominant deformation of an FRCC SENB specimen under fracture is the rigid body rotation. Thus the computation of CZM may be sensitive to the accuracy of the bulk E and ν.

[1] http://www.kuraray-am.com/pvaf/fibers.php.

5. Identification of the CZM

The global response of the fracture test on the FRCC SENB specimens, load P versus CMOD and load P versus displacement, are shown in Figs. 16 and 17, respectively. In both figures, all the curves show multiple vertical short drops. Those are the points when the testing is paused for taking the DIC images. Since the loading is CMOD rate controlled, the P versus CMOD curves are smoother than the P versus d curves. The short load drops are due to the self-readjustment of the fractured specimens under a sustained loading. The DIC images are taken when the load reading is stable, which corresponds to the lower point of the drops. The corresponding load level when the images are taken are recorded and used in the FEM–DIC inverse analysis as the key force boundary conditions. It is noted that the facture of the FRCCs is primarily dominated by fibers pulled out, while there are limited number of fiber fracture based on microscope observation.

As discussed in Section 2.2.3, the deformation fields measured at post-peak range are appropriate for the inverse analysis. In addition, three points are used at different load levels for each specimen, as indicated by the circles in Fig. 16.

The fracture energy can be estimated from area under the load versus load-line displacement curves (Fig. 17). The testing frac-

Table 4
FRCC fracture energy estimated from load versus load–line curves.

	FRCC-0.5	FRCC-1	FRCC-2	FRCC-3
G_F (N/mm)	0.44	0.87	1.90	3.58

tured the specimen completely, however, the area under the unrecorded part of the P versus d curve shall be negligible. In addition, due to the missing part of the curve, the fracture energy estimated will be the lower bound of the actual fracture energy. The computed fracture energies for all specimens are listed in Table 4. This fracture energy will be used to construct the initial CZM guess for the inverse computation. In addition, it can also be a reference of comparison for the computed CZM, which shall have slightly higher fracture energy.

5.1. Displacement fields

A typical post-peak DIC image is shown in Fig. 18. The distance between the two loading point is 60 mm, or 3400 pixels. This corresponds to a camera resolution of 17.7 μm/pixel. Visually the elastic deformation of the specimen cannot be noticed due to the very low cohesive strength to elastic modulus ratio of the FRCC specimen. The figure also illustrates the effectiveness of the groove in constraining the crack path.

An illustration of the displacement fields measured by DIC for the FRCC-1 specimen at the three load levels indicated in Fig. 16 is shown in Fig. 19. As can be seen, the parallelism of the field isolines to the direction of the displacement to be measured shows that the displacement field is dominated by the rigid-body components. As FRCC matrix is very brittle, the post-peak crack tip location does not change significantly, at least it is not indicated from the measurement. To further illustrate the dominance of the rigid-body motion of FRCC bulk material under fracture, the displacement field (horizontal displacement only) of an adhesive bonded polymethylmethacrylate (PMMA) SENB specimen after post-peak [30] is shown in Fig. 20 for comparison. The same experimental procedures, including test setup and DIC computation, have been carried out for these two different materials. From Fig. 20, the high gradient of the displacement field near the crack indicates apparent stress concentration. In addition, compressive strain can also be derived in the upper part of the PMMA specimen. The phenomenological observation of Fig. 20 cannot be derived for the FRCC displacement fields shown in Fig. 19.

5.2. Inverse computation of the CZM

Eight control points are used for the spline that construct the CZM traction–separation curve. Cubic Hermite interpolation is used for the interpolation of the spline. The initial guess of the traction–separation curve for the inverse computation is constructed using the same procedure as described in [30]. Displacement field measured at each load level is used as an individual set to compute the CZM, thus there are three sets of computed traction–separation curves corresponding to the three displacement field measurements. The computed CZM traction–separation curves are shown in Fig. 21 for the FRCC with 0.5%, 1%, 2% and 3% PVA fibers, respectively.

All computed FRCC CZM traction–separation curves show an initially hardening curve followed by an approximately linear softening behavior. The traction–separation curves computed from the two higher loads are more consistent in the computed shape while the one computed at the lowest load deviates from the former two. This may be due to the higher relative error in the DIC computed displacement at lower load levels as the deformation at lower load levels is smaller. The P-CMOD curves shown in Fig. 16 shows an initially linear, then a hardening response before reaching the peak load. The hardening portion of the P-CMOD curve may possibly due to the corresponding hardening behavior of the CZM, which is shown in the computed traction–separation relations (Fig. 21). Numerical examples in [5] compared P-CMOD responses of three SENB fracture specimens with a linear softening, a power-low softening, and a hardening CZMs, respectively. Only the SENB with hardening CZM shows an apparent hardening behavior in the global P-CMOD response. Furthermore, recently, Yang and Fischer [37] observed a hardening relation between fiber bridging stress and crack opening through a direct uniaxial tension test. It was also found that the appropriate CZM for an engineered cementitious composite required a hardening behavior [38]. Therefore, the characteristic of shapes of the computed CZM traction–separation curves conform to these recent studies.

The computed CZM traction–separation curves shown in Fig. 21 can be further smoothed using polynomial least-square fitting. A 4th degree polynomial provides the best fitting for the individual curve. However, the fitting does not provide additional insight to the physics. For the ease of simplicity and comparison, the

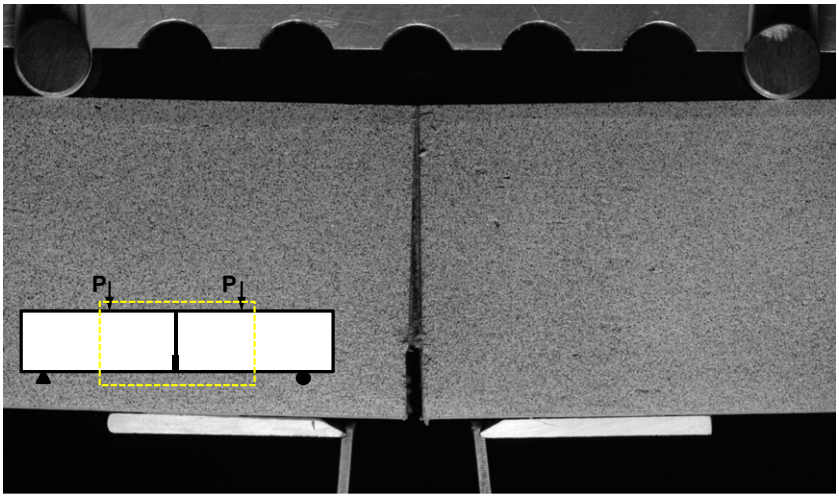

Fig. 18. Typical DIC image of the FRCC SENB taken at a post-peak point. The insert on the left-hand-side indicates the region captured in the photograph.

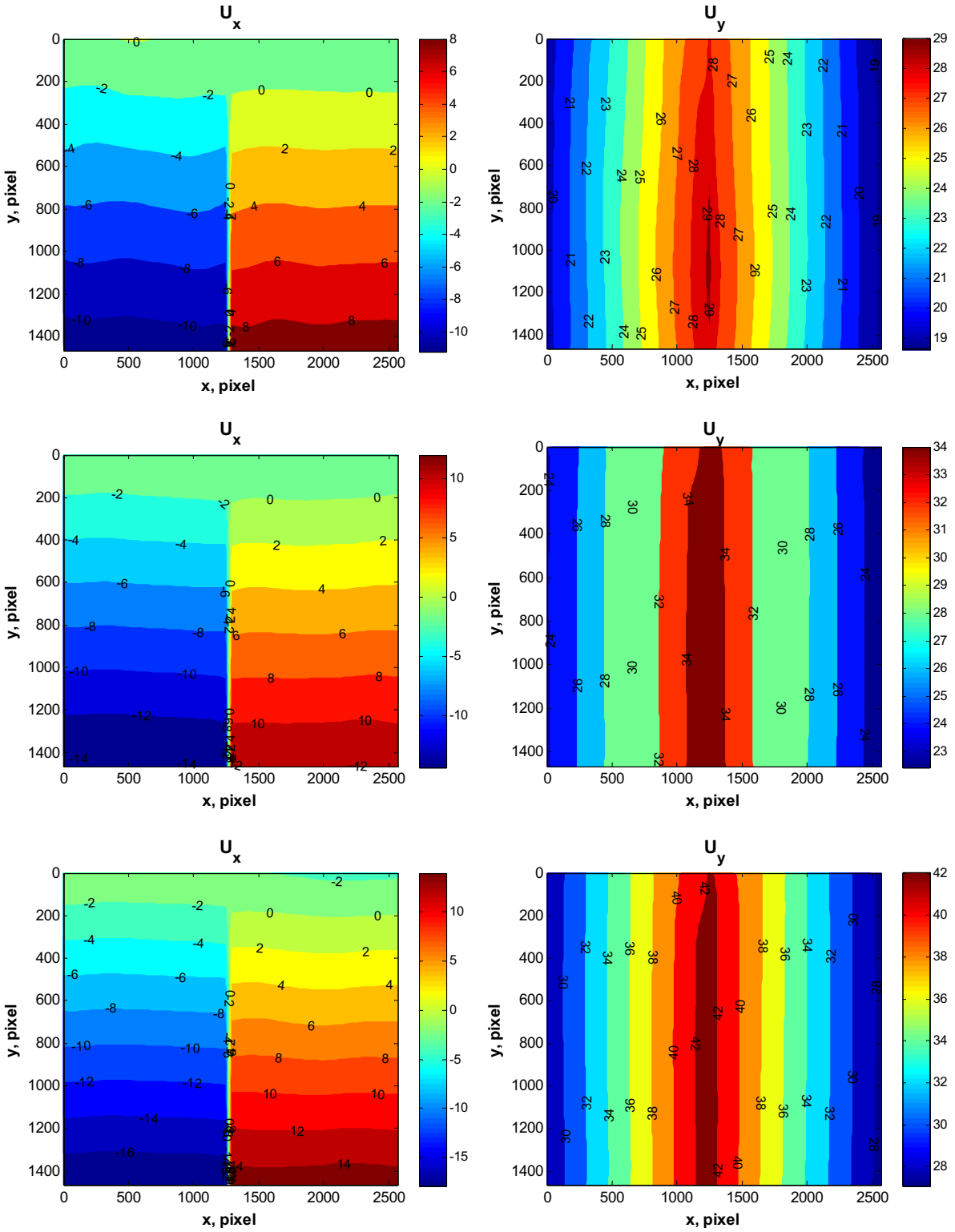

Fig. 19. Displacement field measured by DIC for the FRCC-1 specimen at three post-peak load levels; left: horizontal displacement, right: vertical displacement; measurement unit: pixel.

computed traction–separation curves are averaged using a curve composed of two linear segments, one for the hardening portion and one for the softening portion. To do so, first define a few characteristic parameters. The critical stress σ_{cr} is defined at $\delta = 0$ mm in the computed curves. The cohesive strength $\sigma_{\max}$ is defined as the peak stress of the computed traction–separation curves, and its corresponding COD is defined as δ_p. The critical COD, δ_{cr}, is defined as the separation when the cohesive stress drops to zero. For each of these four parameters, take the average from the three computed traction–separation curves for each FRCC. The averaged

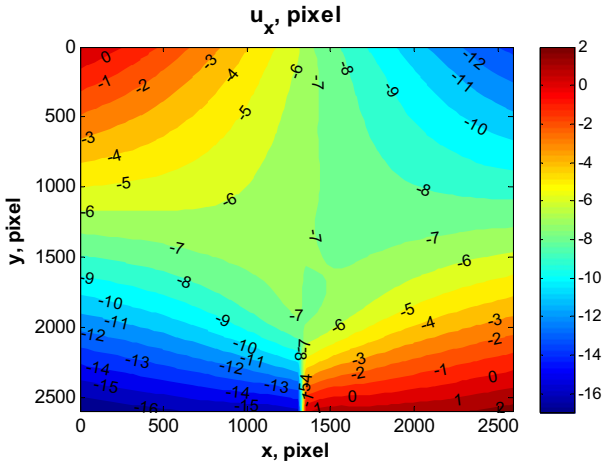

Fig. 20. Displacement field for an adhesive bonded PMMA SENB specimen.

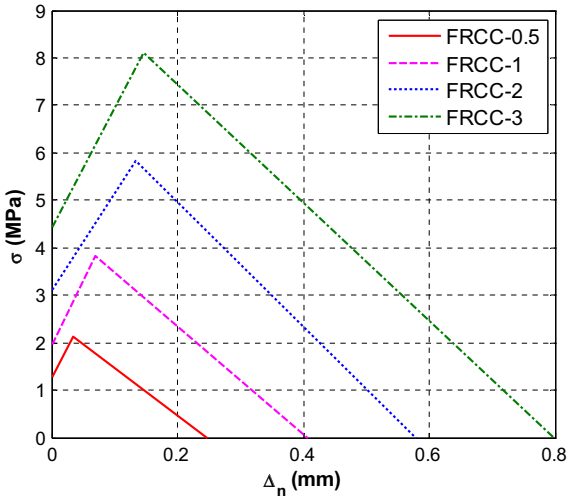

Fig. 22. Comparison of the simplified averaged CZM traction–separation relation of FRCC with different fiber volume fractions.

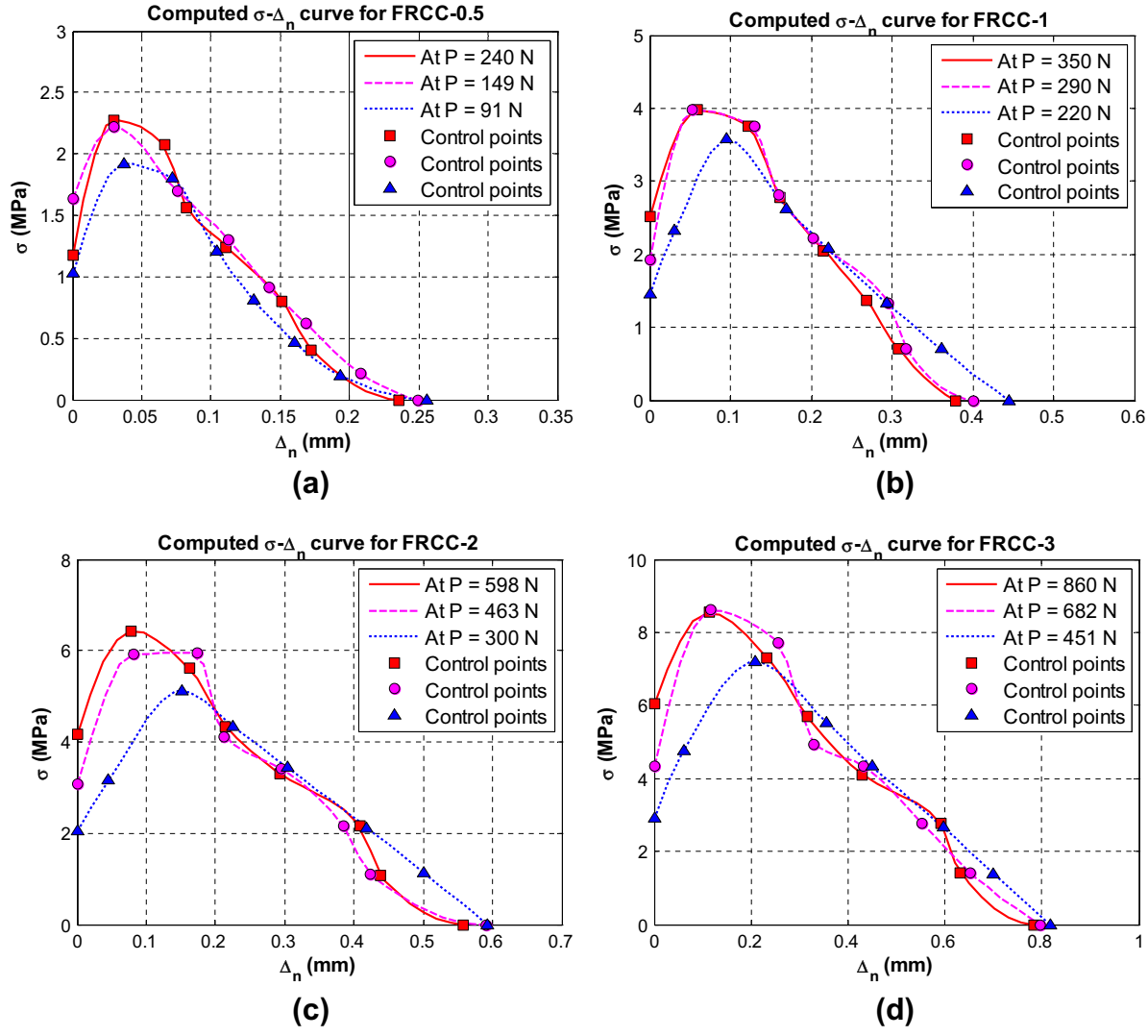

Fig. 21. Inverse computed CZMs for FRCC with: (a) 0.5% PVA fiber, (b) 1% PVA fiber, (c) 2% PVA fiber, and (d) 3% PVA fiber.

Table 5
Critical cohesive stress, critical separation and fracture energy computed CZM; also listed is the fracture energy computed from the global curve.

	FRCC-0.5	FRCC-1	FRCC-2	FRCC-3
σ_{cr} (MPa)	1.277	1.970	3.102	4.421
σ_{max} (MPa)	2.137	3.840	5.834	8.117
Δ_{np} (mm)	0.033	0.069	0.134	0.146
Δ_{nc} (mm)	0.247	0.408	0.580	0.800
G_F, from CZM (N/mm)	0.261	0.860	1.834	3.563
G_F, from P–d curves (N/mm)	0.27	0.87	1.90	3.58

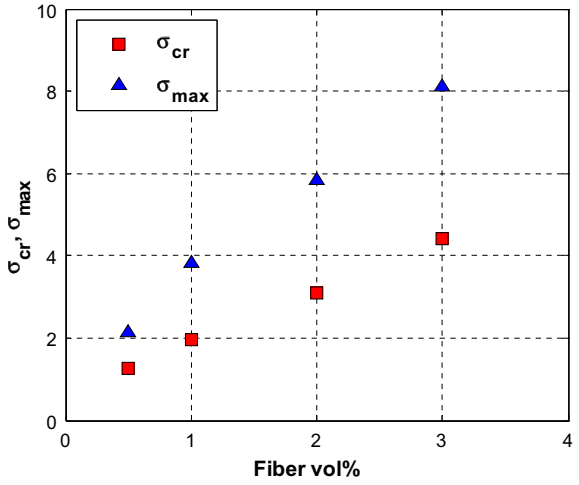

Fig. 23. FRCC critical stress versus fiber volume fraction.

parameters for each FRCC specimen can be used to construct the averaged CZM traction–separation curves by connecting points $(0, \sigma_{cr})$, (σ_{max}, δ_p) and $(\delta_{cr}, 0)$. The averaged CZM traction–separation curves for all FRCC specimens are shown in Fig. 22.

The averaged parameters that characterize the CZMs and the fracture energy are also listed in Table 5. The critical stress of the FRCC has a linear relation with respect to fiber volume fraction (Fig. 23). This is expected as the tensile strength of FRCC is controlled by the volume fraction of the fibers. On the other hand, the fracture resistance also increases with increasing fiber volume fraction. Such effect is reflected in the averaged CZM model as the increased critical stress. The increase of critical separation with fiber volume fraction conforms to the increased ultimate CMOD measured (Fig. 16). Table 5 also shows the fracture energy computed from global response curve, P versus d. The fracture energies computed from two very different methods are close (Fig. 24), except for FRCC-0.5. It has been explained that the fracture energy from computed traction–separation curve shall be higher than the one computed from P versus d curve. If only the traction–separation relation computed from the highest load is used to compute the fracture energy, the value will be slightly higher and may be more reasonable. The fracture energy is also proportional to the fiber volume fraction, which is expected as the cement matrix has negligible fracture energy comparing to the fracture energy contributed by the PVA fibers.

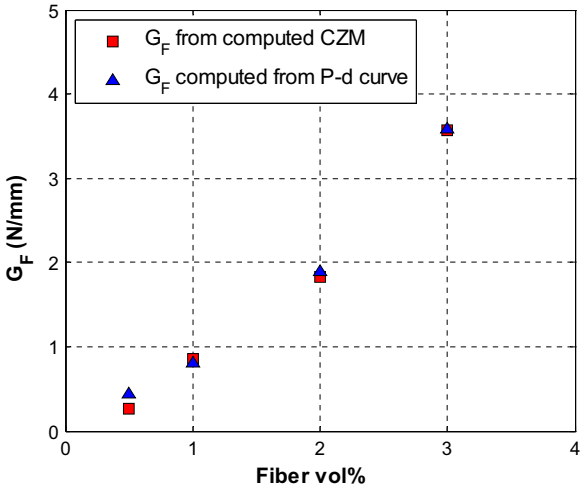

Fig. 24. Fracture energy versus fiber volume fraction.

5.3. Direct simulation using the computed CZM

The computed CZMs is verified by means of its use in direct simulations to obtain the global response and compared with the experimental measurements. Since only a few snapshots of the experimental points are used, but not the global response, e.g., P versus CMOD, in the computation of the CZMs, thus verification by comparing to the global response is somewhat justified. The simulated P versus CMOD curves are plotted together and shown in Fig. 25.

It can be seen from Fig. 25 that the computed results conform well to the experimental results. Notice the particular good match of the curves for the softening part of the curves. The initial portion of the curves is only elastic, and the FEM simulations match well with the experiments, which indicate that the identified Young's modulus and Poisson's ratio are good estimates.

6. Conclusions

The identification of elastic moduli (Young's modulus and Poisson's ratio) and CZM of homogeneous PVA microfiber reinforced cementitious composites is carried out in this study. Both identification problems use the full displacement field computed by DIC as the input to an FEM based inverse problem formulation. The robust FEM Update method is used for the optimization.

For the identification of the elastic moduli, four-point bend tests are used. The linearized Hooke's tensor is derived for isotropic material at plane stress condition. An efficient Newton–Raphson solver is used. The computed elastic moduli for the FRCCs with different fiber volume fractions (0.5–3%) are between 17.6 and 20.4 GPa, while the computed Poisson's ratios are within the range from 0.141 to 0.150. The computed elastic moduli are consistent with data reported in the literature. The presence of PVA fibers slightly affects the modulus of elasticity while it does not affect the Poisson's ratio apparently.

For the identification of the CZM, SENB specimens are used. DIC displacements are obtained from three post-peak load levels. The CZMs computed at these different load levels are consistent. The shapes of computed CZMs for the FRCCs all show an initial hardening followed by an approximately linear softening behavior. This is because, after the cement matrix cracks, the PVA fibers govern the crack opening process and the fiber bridging action contributes to the increase of cohesive stress and fracture energy. The fracture toughness is contributed primarily by the PVA fibers. It is found that the cohesive strength and the fracture energy have a linear relation to the fiber volume fraction. It is also found that the computed critical separation also increases with the increase of fiber volume fraction. The fracture energy computed from the CZM is consistent with those computed from the global load versus

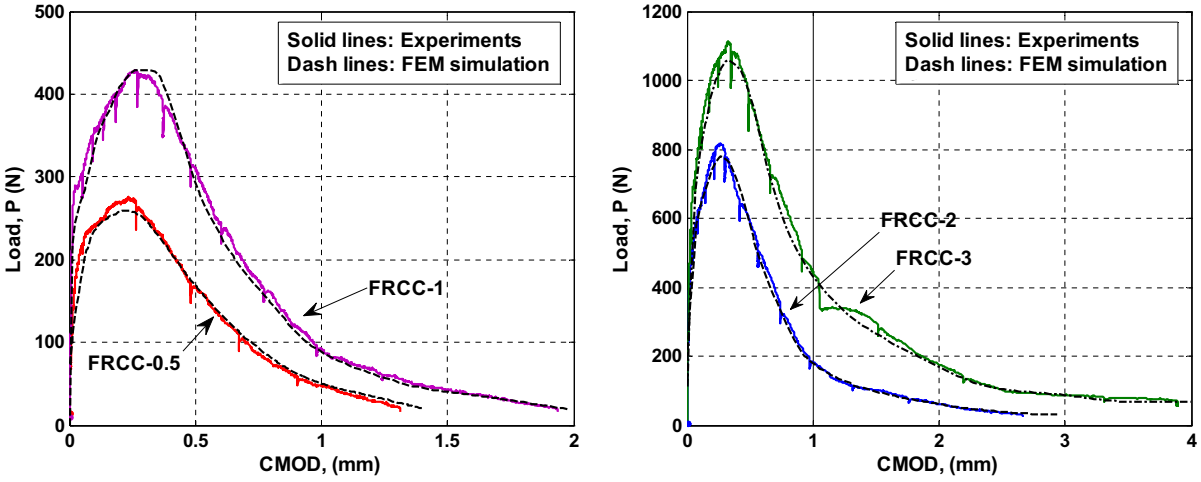

Fig. 25. Comparison of experiment and FEM simulation of the *P* versus CMOD curves (FEM simulation use the inverse computed CZMs).

load–line displacement. The direct simulation using the computed CZMs yields consistent global responses in comparison with the experimental measurements.

References

[1] Barenblatt GI. The formation of equilibrium cracks during brittle fracture. General ideas and hypotheses. Axially-symmetric cracks. J Appl Math Mech 1959;23(3):622–36.

[2] Dugdale DS. Yielding of steel sheets containing slits. J Mech Phys Solids 1960;8(2):100–4.

[3] Song SH, Paulino GH, Buttlar WG. Influence of the cohesive zone model shape parameter on asphalt concrete fracture behavior. In: Paulino GH, Pindera M-J, Dodds Jr RH, Rochinha FA, V DE, Chen L, editors. Multiscale and functionally graded materials. Oahu Island (Hawaii): AIP; 2008. p. 730–5.

[4] Volokh KY. Comparison between cohesive zone models. Commun Numer Methods Eng 2004;20(11):845–56.

[5] Shen B. Functionally graded fiber-reinforced cementitious composites – manufacturing and extraction of cohesive fracture properties using finite element and digital image correlation, Ph.D. Thesis. United States, University of Illinois at Urbana–Champaign; 2009.

[6] Shen B, Stanciulescu I, Paulino GH. Inverse computation of cohesive fracture properties from displacement fields. Inverse Problems Sci Eng 2010;18: 1103–28.

[7] van Mier JGM. Fracture processes of concrete: assessment of material parameters for fracture models. Boca Raton: CRC Press; 1997.

[8] Elices M. The cohesive zone model: advantages, limitations and challenges. Eng Fract Mech 2002;69(2):137–63.

[9] Seung Hee K, Zhifang Z, Shah SP. Effect of specimen size on fracture energy and softening curve of concrete: Part II. Inverse analysis and softening curve. Cem Concr Res 2008;38(8-9):1061–9.

[10] Slowik V, Villmann B, Bretschneider N, Villmann T. Computational aspects of inverse analyses for determining softening curves of concrete. Comput Methods Appl Mech Eng 2006;195(52):7223–36.

[11] de Oliveira e Sousa JLA, Gettu R. Determining the tensile stress–crack opening curve of concrete by inverse analysis. J Eng Mech 2006;132(2):141–8.

[12] Tan H, Liu C, Huang Y, Geubelle PH. The cohesive law for the particle/matrix interfaces in high explosives. J Mech Phys Solids 2005;53(8):1892–917.

[13] Dally JW, Riley WF. Experimental stress analysis. Knoxville (Tenn): College House Enterprises; 2005.

[14] Peters WH, Ranson WF. Digital imaging techniques in experimental stress analysis. Opt Eng 1982;21(3):427–31.

[15] Sutton MA, Wolters WJ, Peters WH, Ranson WF, McNeill SR. Determination of displacements using an improved digital correlation method. Image Vision Comput 1983;1(3):133–9.

[16] Chu TC, Ranson WF, Sutton MA, Peters WH. Applications of digital-image-correlation techniques to experimental mechanics. Exp Mech 1985;25(3):232–44.

[17] Bruck HA, McNeill SR, Sutton MA, Peters III WH. Digital image correlation using Newton–Raphson method of partial differential correction. Exp Mech 1989;29(3):261–7.

[18] Abanto-Bueno J, Lambros J. Investigation of crack growth in functionally graded materials using digital image correlation. Eng Fract Mech 2002;69(14–16):1695–711.

[19] Abanto-Bueno J, Lambros J. Experimental determination of cohesive failure properties of a photodegradable copolymer. Exp Mech 2005;45(2):144–52.

[20] Bonnet M, Constantinescu A. Inverse problems in elasticity. Inverse Problems 2005;21(2):1–50.

[21] Avril S, Bonnet M, Bretelle A-S, Grediac M, Hild F, Ienny P, et al. Overview of identification methods of mechanical parameters based on full-field measurements. Exp Mech 2008;48(4):381–402.

[22] Choi S, Shah SP. Measurement of deformations on concrete subjected to compression using image correlation. Exp Mech 1997;37(3):307–13.

[23] Sokhwan C, Shah SP. Fracture mechanism in cement-based materials subjected to compression. J Eng Mech – ASCE 1998;124(1):94–102.

[24] Corr D, Accardi M, Graham-Brady L, Shah SP. Digital image correlation analysis of interfacial debonding properties and fracture behavior in concrete. Eng Fract Mech 2007;74(1–2):109–21.

[25] Molimard J, Le Riche R, Vautrin A, Lee JR. Identification of the four orthotropic plate stiffnesses using a single open-hole tensile test. Exp Mech 2005;45(5):404–11.

[26] Zhang Z, Paulino GH. Cohesive zone modeling of dynamic failure in homogeneous and functionally graded materials. Int J Plast 2005;21(6):1195–254.

[27] Fletcher R. Practical methods of optimization. Chichester; New York: Wiley; 1987.

[28] Nelder JA, Mead R. Simplex method for function minimization. Comput J 1965;7(4):308–13.

[29] Nocedal J, Wright SJ. Numerical optimization. New York: Springer; 2006.

[30] Shen B, Paulino GH. Direct extraction of cohesive fracture properties from digital image correlation: a hybrid inverse technique. Exp Mech 2011;51(2): 13–63.

[31] Park K, Paulino GH, Roesler JR. Determination of the kink point in the bilinear softening model for concrete. Eng Fract Mech 2008;75(13):3806–18.

[32] Shen B, Hubler M, Paulino GH, Struble LJ. Functionally-graded fiber-reinforced cement composite: processing, microstructure, and properties. Cem Concr Compos 2008;30(8):663–73.

[33] Mehta PK, Monteiro PJM. Concrete: microstructure, properties, and materials. 3rd ed. New York: McGraw-Hill; 2006.

[34] Mindess S, Young JF, Darwin D. Concrete. 2nd ed. Upper Saddle River (NJ): Prentice Hall; 2003.

[35] Shao Y, Shah SP. Mechanical properties of PVA fiber reinforced cement composites fabricated by extrusion processing. ACI Mater J 1997;94(6): 555–64.

[36] Li VC, Wang S, Wu C. Tensile strain-hardening behavior or polyvinyl alcohol engineered cementitious composite (PVA–ECC). ACI Mater J 2001;98(6): 483–92.

[37] Yang J, Fischer G. Simulation of the tensile stress–strain behavior of strain hardening cementitious composites. In: Konsta-Gdoutos MS, editor. Measuring, monitoring and modeling concrete properties. Dordrecht: Springer; 2006. p. 25–31.

[38] Dick-Nielsen L, Stang H, Poulsen PN. Condition for strain-hardening in ECC uniaxial test specimen. In: Konsta-Gdoutos MS, editor. Measuring, monitoring and modeling concrete properties. Dordrecht: Springer; 2006. p. 41–7.